Processing of Very High Resolution GF-3 SAR Spotlight Data With Non-Start–Stop Model and Correction of Curved Orbit

Da Liang , *Student Member, IEEE*, Heng Zhang , *Member, IEEE*, Tingzhu Fang , Yunkai Deng, *Member, IEEE*, Weidong Yu, *Member, IEEE*, Lei Zhang, and Huaitao Fan , *Member, IEEE*

Abstract—A novel imaging algorithm is presented in this article for focusing the very high resolution spaceborne synthetic aperture radar (SAR) data of spotlight mode. The long synthetic aperture time in spotlight mode brings new problems, such as Doppler spectrum aliasing and curved orbit. The imaging results will be filled with ambiguity and would suffer from resolution reduction if Doppler spectrum aliasing is not handled. The error introduced by curved orbit will degrade resolution of the target and introduces asymmetric sidelobes in azimuth direction. The start–stop approximation is no longer applicable, since it introduces two effect, e.g., "fast-time" effect and "slow-time" effect, which will cause defocusing and range-dependent azimuth shift, respectively if not handled. The proposed algorithm combines the two-steps processing approach (TSPA) and the backprojection algorithm (BPA). First, the initial step of TSPA is used to get a high azimuth sampling rate which is higher than pulse repetition frequency to avoid the Doppler spectrum aliasing. Then, the "fast-time" effect of start–stop approximation is corrected in the 2-D frequency domain. Finally, the BPA is used to correct the error introduced by the curved orbit and the "slow-time" effect of start–stop approximation. The experimental results of spaceborne SAR data acquired by Gaofen-3 (GF-3) SAR system demonstrate the feasibility of the proposed algorithm.

Index Terms—Backprojection algorithm (BPA), spotlight, synthetic aperture radar (SAR), two-steps processing.

I. INTRODUCTION

SYNTHETIC aperture radar (SAR) is an important remote sensing tool which has been widely used for earth observation operating in all day and all weather conditions [1]. Modern

Da Liang and Tingzhu Fang are with the Space Microwave Remote Sensing System Department, Aerospace Information Research Institute, Chinese Academy of Sciences, Beijing 100094, China, and also with the School of Electronic, Electrical and Communication Engineering, University of Chinese Academy of Sciences, Beijing 100049, China (e-mail: daliang16@foxmail.com; fangtingzhu17@mails.ucas.ac.cn).

Heng Zhang, Yunkai Deng, Weidong Yu, Lei Zhang, and Huaitao Fan are with the Space Microwave Remote Sensing System Department, Aerospace Information Research Institute, Chinese Academy of Sciences, Beijing 100094, China (e-mail: caszhmail@163.com; ykdeng@mail.ie.ac.cn; ywd@mail.ie.ac.cn; 314forever@163.com; huaitaofan@163.com).

TABLE I
OBSERVATION MODES OF GF-3

#	Imaging Modes	Resolution(m) Azimuth	Range	Nominal Swath(km)
1	Spotlight	1.0~1.5	0.9~2.5	10×10^{1}
2	Ultra-fine strip	3	2.5~5	30
3	Fine strip I	5	4~6	50
4	Fine strip II	10	8~12	100
4	Standard strip	25	15~30	130
6	Narrow scan	50~60	30~60	300
7	Wide scan	100	50~110	500
8	Global	500	350~700	650
9	Quad-pol strip I	8	6~9	30
10	Quad-pol strip II	25	15~30	40
11	Wave	10	8~12	5×5[1]
12	Extended low	25	15~30	130
12	Extended high	25	20~30	80

[1]Image is discontinuous in azimuth, ×10 and ×5 refer to the azimuth length in one acquisition.

SAR systems are characterized by high resolution and wide swath coverage [2]–[5]. The range and azimuth resolutions are determined by the bandwidth of the transmitted signal and the length of the synthetic aperture, respectively. In order to obtain a high resolution in range, large bandwidth signals are necessary. The spotlight mode offers the possibility of a very high geometric resolution in the azimuth direction [6].

The Gaofen-3 (GF-3) satellite was launched on August 10, 2016, which is the first multipolarization C-band SAR imaging satellite of China [7]–[9]. As one of the most important satellites in the China's Earth Observation System, GF-3 has the characteristics of high resolution, large imaging width, high radiometric precision, and multi-imaging mode [10]. GF-3 SAR can be separated into 12 observing modes by different resolution and swath, such as spotlight mode, ultrafine stripmap, wide scanSAR mode, and so on [7], [11]–[13], as shown in Table I. GF-3 not only plays an important role in the fields of marine environment monitoring, resource investigation, disaster prevention, and water conservancy but also provides high-quality data for scientific experiments [11]. In order to exploit the maximum azimuth steering capability of the GF-3 SAR system, spotlight experiments were performed after the satellite had been in operational mode [14].

The capabilities of high azimuth resolution in the spotlight mode are accompanied by new challenges. The first problem

is Doppler spectrum aliasing. Due to azimuth antenna beam steering in the spotlight mode, the total Doppler bandwidth will exceed several pulse reception frequency (PRF) intervals [2]. The imaging results will be filled with ambiguity and would suffer from resolution reduction if Doppler spectrum aliasing is not handled. To solve the Doppler spectrum aliasing in the spotlight mode, a number of imaging algorithms have been developed, and they can generally be classified into subaperture [2], [15]–[18] and full aperture approaches [19]–[22]. The subaperture approach first divides the raw data into subapertures in the azimuth time domain. In each subaperture, the spectrum width of azimuth is less than PRF. As a result, the spectrum aliasing is overcome in each subaperture. Then, high resolution is obtained by synthesizing the coarse-resolution images of each subaperture. The two-step processing approach (TSPA) proposed in [19] and [20] is a typical full aperture approach. The key point of this technique is the azimuth convolution between the raw data and the selected chirp signal implemented by two times of complex matrix multiplication and a discrete Fourier transform via efficient fast Fourier transform (FFT) [22].

Another induced problem is the curved orbit [23]. When the azimuth resolution is low, the synthetic aperture time is short. In this case, the second-order approximation of range history is sufficient. The error introduced by third- and higher-order terms of range history can be ignored in the analysis. Therefore, the acquisition geometry of SAR can be depicted by the hyperbolic range equivalent model (HREM) or the equivalent squinted range model [2], [17], [24]–[26]. However, when the azimuth resolution is high, the synthetic aperture time is long, the error introduced by third- and higher-order terms of range history cannot be ignored. As [15] shows, the third- and higher-order terms would introduce more than 200-degree phase error for TerraSAR spotlight mode with synthetic aperture time of 7 s. In [27], the fourth-order model Doppler range model (DRM4) was proposed to compensate the third- and fourth-order phase errors, but it does not consider the effect of higher-order errors, which limits its application.

The third problem is the motion of the satellite between the transmission and reception of the signal. The start–stop approximation is used in the conventional imaging algorithms [2], [20]. However, under certain circumstances, using the start–stop approximation may result in a significant error [28]. For example, as stated in [15], for the TerraSAR-X SAR, if the error brought by the start–stop approximation is not corrected, it would introduces resolution loss of up to 15%. The start–stop approximation introduces two effects, i.e., "fast-time" effect and "slow-time" effect, which will cause defocusing if not handled. To address this problem, the method based on a phase correction function in the 2-D frequency domain was proposed in [15]. A modified backprojection algorithm (BPA) was also proposed to correct the error introduced by the start–stop approximation in [29].

For high resolution spaceborne SAR system, all the problems mentioned above should be considered. The method proposed in [15] gives a generic processing flow. It applied the range history of a reference target in the swath center to compensate

for echo phase to be purely hyperbolic. However, this method cannot be applied to the imaging of large swaths. The time domain algorithm, backprojection algorithm , can be applied to almost every SAR configuration [30]–[32]. The immense time cost limits its application. However, with the development of parallel computing platform with incredible computing power, e.g., general-purpose graphics processing unit, the acceleration of the progress of the BPA is huge [33]–[35]. Another advantage is that the BPA can handle the problem of the curved orbit. Also, the BPA can correct "slow-time" effect introduced by start–stop approximation since it can regard monostatic SAR as bistatic SAR with separation of transmitting signal position and receiving position [36].

In this article, an imaging algorithm combined with TSPA and BPA is proposed for very high resolution spaceborne SAR data processing. First, the initial step of TSPA is used to get a high azimuth sampling rate which is higher than PRF for the raw data. Then, the "fast-time" effect of start–stop approximation is corrected in 2-D frequency domain. Finally, the BPA is used to correct the error introduced by the curved orbit and the "slow-time" effect of start–stop approximation. A simulation for the spaceborne spotlight SAR with 0.2 m azimuth resolution is given to illustrate the significant error introduced by the curved orbit and the start–stop approximation. The simulation result shows that, by using conventional processing, we cannot obtain a satisfactory image quality. However, by using the proposed algorithm, an image with high focusing quality can be obtained. The GF-3 data experiment also demonstrates the feasibility of the proposed method. The antenna pattern, topography dependence, and atmospheric effects, which should be considered in very high-resolution spaceborne SAR, have been systematically discussed in [14], [16], and [37], thus, they are not explained in detail in the article.

The rest of this article is organized as follows. The error analysis of hyperbolic approximation and the non-start–stop model are presented in Section II. An algorithm based on the TSPA and BPA is proposed to compensate the errors brought by the start–stop model and curved orbit accurately. The proposed algorithm is described in detail in Section III. In Section IV, the simulation experiment and the spaceborne SAR data experiment demonstrate the feasibility of the proposed algorithm. Section V concludes this article.

II. ECHO MODEL OF SPACEBORNE SAR

In spotlight mode, the beam is steered to illuminate the common spot on the ground, therefore, a larger synthetic aperture can be formed, and a higher azimuth resolution is obtained. The geometry of the spotlight mode is shown in Fig. 1. Spotlight SAR is capable of extending the high-resolution SAR imaging capability significantly. Due to the long integration time in high resolution spaceborne spotlight mode, the trajectory of SAR is not a straight line. In this section, the curved orbit is introduced. The non-start–stop model is also introduced for very high-resolution spaceborne SAR. The echo model of spaceborne SAR is described in detail.
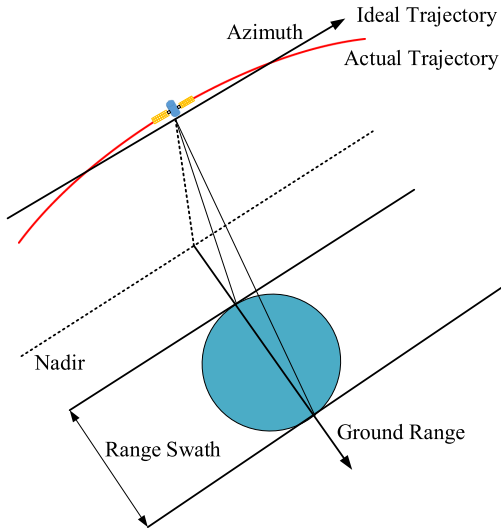
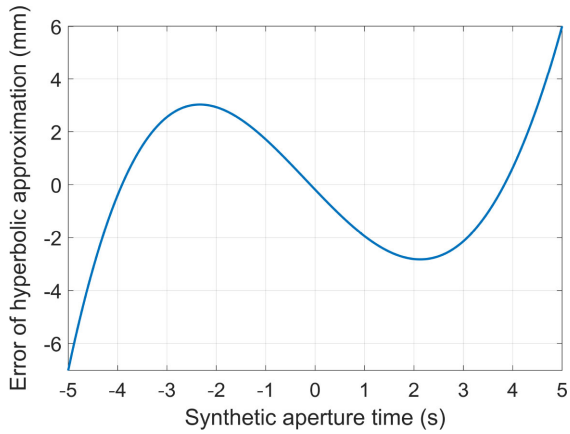Fig. 1.   Imaging geometry of the spaceborne spotlight mode.

Fig. 2.   Error of the hyperbolic approximation using an effective velocity.

A. Curved Orbit

In spaceborne SAR system, the satellite's flight path as well as the earth's surface are curved, and the earth rotates continuously. The HREM is derived from the straight track and can be adapted to the curved orbit of spaceborne SAR by using the concept of equivalent velocity. However, the HREM becomes less accurate in the condition of large integration time. For example, as Fig. 2 shows, if the spotlight mode has an integration time of about 10 s, the maximum error of hyperbolic approximation will reach 6 mm [15]. Such an error degrades the azimuth resolution and introduces asymmetric sidelobes. To get well-focused imagery from the high-resolution spotlight SAR mode, the error introduced by the curved orbit should be definitely corrected.

B. Non-Start–Stop Model

The start–stop approximation in the SAR image formation literature has assumed that the radar does not move during the transmission of the signal. This approximation has been
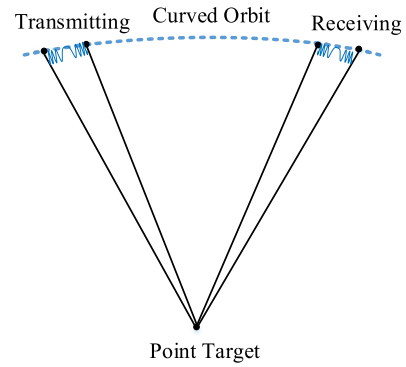

Fig. 3.   Non-start–stop model.

thought particularly suitable for low-resolution SAR. However, in high-resolution SAR systems, the start–stop approximation may introduce significant errors. The start–stop approximation has mainly two effects [15]. A "slow-time" one is linked to the fact that the satellite indeed moved between transmission and reception. A "fast-time" one deals with the motion of the satellite during the transmission and reception of the chirp signal [15],[29],[38], as illustrated in Fig. 3. This effect will introduce a range-azimuth coupling phase term in 2-D-frequency domain [14], [38].

Here, the non-start–stop model is used to simulate the continuous motion of the satellite. The key of this method is to acquire an accurate transmitting distance according to the receiving distance for every echo sampling point [28]. By performing the iteration method for every sampling point, the transmitting and receiving distance can precisely be calculated and substituted to form the simulated echoes.

C. Echo Model

Because the curved orbit and non-start–stop model are all considered in the processing of spaceborne SAR data, the range history $R(\tau, \eta)$ between the radar and the target is a function of the range time τ and the azimuth time η. Then, the demodulated baseband signal from a single point target can be represented as [25]

$$S_0(\tau, \eta) = A_0 w_r \left[\tau - \frac{2R(\tau, \eta)}{c} \right] w_a(\eta)$$

$$\times \exp\left[-j\frac{4\pi R(\tau, \eta)}{\lambda} \right] \exp\left[j\pi K_r \left(\tau - \frac{2R(\tau, \eta)}{c} \right)^2 \right]$$

(1)

where A_0 is a complex constant, c is the speed of light, λ is the wavelength of carrier frequency, K_r is the chirp rate of the transmitted signal, w_r is range envelope, and w_a is azimuth envelope.

III. PROPOSED PROCESSING FLOW

An imaging algorithm for very high resolution spaceborne SAR data is proposed in this section. The key procedures are
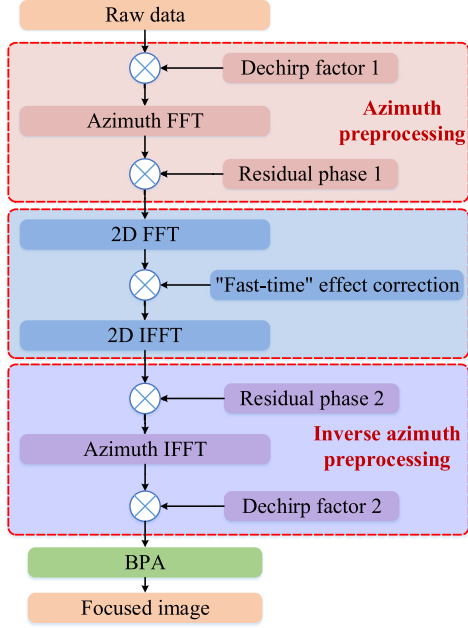
Fig. 4.   Framework of the proposed algorithm.

discussed in detail. The whole algorithm contains four steps. First, the initial step of TSPA is used to get a high sampling rate in azimuth. Second, a filter is used to correct the "fast-time" effect in the start–stop approximation. Third, the data are transformed into the same format as raw data, which can be regarded as the inverse processing of the initial step of TSPA. Finally, the BPA is used to get the final image. The flowchart of the proposed algorithm is shown in Fig. 4.

A. Azimuth Preprocessing

In spotlight mode, the Doppler bandwidth of a target located in the scene is usually much larger than the PRF. As a result, the azimuth spectral aliasing phenomenon occurs. Here, the initial step of TSPA is used to get a high azimuth sampling rate which is higher than PRF [20]. This step involves an azimuth convolution and zero-padding in azimuth. The selected chirp signal $S_{\text{ref}}(\eta)$ in the azimuth convolution is as follows:

$$S_{\text{ref}}(\eta) = \exp(j\pi K_a \eta^2) \tag{2}$$

where K_a is the Doppler frequency modulation rate of the reference point in the scene, and it can be expressed as

$$K_a = \frac{2v_r^2}{\lambda r} \tag{3}$$

where the r is the range of the reference point in the illuminated scene, v_r is the equivalent velocity of the HREM. The signal $S_1(\tau, \eta)$ is obtained by convolution of the raw data $S_0(\tau, \eta)$ and the reference chirp signal $S_{\text{ref}}(\eta)$

$$S_1(\tau, \eta) = S_0(\tau, \eta) \otimes_{az} S_{\text{ref}}(\eta) = S_0(\tau, \eta) \otimes_{az} \exp(j\pi K_a \eta^2). \tag{4}$$

The azimuth signal is obviously compressed after the azimuth convolution operation. Accordingly, by neglecting inessential complex amplitude factors, in the discrete domain, (4) can be expressed as follows:

$$S_1(\tau, n \cdot \Delta\eta')$$

$$= \sum_{i=-I/2}^{I/2-1} S_0(\tau, i \cdot \Delta\eta) \cdot S_{\text{ref}}(n \cdot \Delta\eta' - i \cdot \Delta\eta)$$

$$= \exp\left[j\pi K_a(n \cdot \Delta\eta')^2\right] \sum_{i=-I/2}^{I/2-1} S_0(\tau, i \cdot \Delta\eta)$$

$$\cdot \exp\left[j\pi K_a(i \cdot \Delta\eta)^2\right] \cdot \exp\left(-j2\pi K_a in\Delta\eta\Delta\eta'\right)$$

$$\text{with } n = -P/2, \ldots, P/2 - 1 \tag{5}$$

where I is the number of input azimuth samples, $\Delta\eta = 1/PRF$ is the azimuth data sampling interval, $\Delta\eta'$ is the output azimuth data sampling interval, and P is the number of output azimuth samples. The relationship between $\Delta\eta$ and $\Delta\eta'$ can be written as

$$\Delta\eta' = \frac{1}{PK_a\Delta\eta}. \tag{6}$$

The adopted azimuth convolution can be implemented by two times of complex matrix multiplication and an azimuth FFT.

B. Correction of the "Fast-Time" Effect

The "fast-time" effect is caused by the motion of the satellite during the transmission and reception of the chirp signal. In order to deal with the "fast-time" effect in start–stop approximation, the following filter is used to compensate the error in the 2-D frequency domain [15]:

$$H(f_\tau, f_\eta) = \exp\left(-j2\pi \frac{f_\eta}{K_r} f_\tau\right) \tag{7}$$

where f_τ is the range frequency and f_η is the azimuth frequency. The signal $S_2(f_\tau, f_\eta)$ in 2-D-frequency domain can be expressed as

$$S_2(f_\tau, f_\eta) = S_1(f_\tau, f_\eta)H(f_\tau, f_\eta). \tag{8}$$

C. Inverse Azimuth Preprocessing

After the correction of "fast-time" effect in start–stop approximation, the signal $S_2(\tau, \eta)$ is transformed into signal $S_3(\tau, \eta)$ by inverse azimuth preprocessing. The signal $S_3(\tau, \eta)$ can be expressed as

$$S_3(\tau, \eta) = S_2(\tau, \eta) \otimes_{az} \text{conj}(S_{\text{ref}}(\eta))$$

$$= S_2(\tau, \eta) \otimes_{az} \exp(-j\pi K_a \eta^2) \tag{9}$$

where the $\text{conj}(\cdot)$ represents the conjugate of the complex number. Equation (9) can be regarded as the inverse processing of (4).

In the discrete domain, it can be written as

$$S_3(\tau, i \cdot \Delta\eta)$$

$$= \sum_{n=-P/2}^{P/2-1} S_2(\tau, n \cdot \Delta\eta') \cdot \text{conj}(S_{\text{ref}}(i \cdot \Delta\eta - n \cdot \Delta\eta'))$$

$$= \exp\left[-j\pi K_a(i \cdot \Delta\eta)^2\right] \sum_{n=-P/2}^{P/2-1} S_2(\tau, n \cdot \Delta\eta')$$

$$\cdot \exp\left[-j\pi K_a(n \cdot \Delta\eta')^2\right] \cdot \exp(j2\pi K_a i n \Delta\eta \Delta\eta')$$

$$\text{with } i = -I/2, \cdots I/2 - 1. \tag{10}$$

D. Backprojection Algorithm

Since the new raw data are processed with the correction of the "fast-time" effect, the range history $R(\tau, \eta)$ is only a function of the slow time η. As a result, the range history $R(\tau, \eta)$ can be written as $R(\eta)$. Due to the motion of satellite between transmission and reception, the transmitting position and receiving position are different. Therefore, the distance $R_T(\eta)$ between the transmitting position and the target and the distance $R_R(\eta)$ between the receiving position and the target are not equal. The $R(\eta)$ can be expressed as

$$R(\eta) = R_T(\eta) + R_R(\eta). \tag{11}$$

Then, the BPA is used to deal with the curved orbit and the "slow-time" effect in start–stop approximation. Because BPA is a point-by-point reconstruction method, it can correct the errors brought by the curved orbit and the "slow-time" effect in start–stop approximation. The BPA integrates the product of echo signals and reference phase to get a focused point target $g(\boldsymbol{x})$ which can be written as

$$g(\boldsymbol{x}) = \int S_{3\_\text{comp}}\left(\frac{R(\eta)}{c}, \eta\right) \exp\left(j\frac{2\pi R(\eta)}{\lambda}\right) d\eta \tag{12}$$

where the $S_{3\_\text{comp}}(\tau, \eta)$ denotes data $S_3(\tau, \eta)$ after range compression and $\boldsymbol{x}$ denotes the position of a target in the illuminated scene. In the processing of the signal $S_3(\tau, \eta)$ by using BPA, the graphics processing unit is used to enhance the efficiency of the BPA since the BPA calls for high computation [33], [39]. NVIDIA P100 is used in the experiment.

E. Analysis of Computational Load

This part mainly analyzes the computational load of TSPA and the proposed algorithm. Suppose N_r is the number of range samples, and I and N_r denote the azimuth and range pixel numbers of the final image, respectively. The initial step of TSPA requires

$$N_{\text{ini\_TSPA}} = N_r I + N_r P \log_2 P + N_r P \tag{13}$$

operations. Using the computational load of standard chirp scaling algorithm $(2 \log_2 P + 2 \log_2 N_r + 3)N_r P$ for reference [25], the computational load of TSPA can be expressed
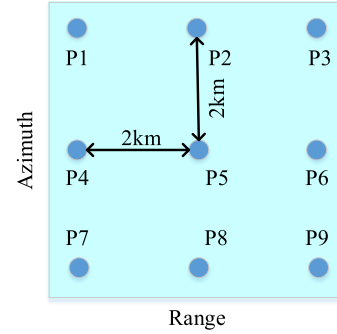

Fig. 5. Point targets in ground scene for simulation.

as

$$N_{\text{TSPA}} = N_r I + 4N_r P + 3N_r P \log_2 P + 2N_r P \log_2 N_r. \tag{14}$$

The computational load of inverse azimuth preprocessing is equal to $N_{\text{ini\_TSPA}}$. The computational load of correction of the "fast-time" effect is $N_{\text{correct}} = (2 \log_2 P + 2 \log_2 N_r + 1)N_r P$. The computational load of BPA can be expressed as

$$N_{\text{BPA}} = IN_r \log_2 N_r + IN_r + IKN_r \log_2(KN_r) + I^2 N_r \tag{15}$$

where K is the up-sampling ratio. Therefore, the computational load of the proposed algorithm can be represented as

$$N_{pro\_alg} = 2N_{\text{ini\_TSPA}} + N_{\text{correct}} + N_{\text{BPA}}$$

$$= 3N_r I + 4N_r P \log_2 P + 2N_r P \log_2 N_r + 3N_r P$$

$$+ IN_r \log_2 N_r + IKN_r \log_2(KN_r) + I^2 N_r. \tag{16}$$

IV. EXPERIMENT

In this section, the simulation experiments are carried out to validate the proposed algorithm. Then, the results based on the spaceborne SAR data acquired by GF-3 SAR system are demonstrated.

A. Results of Simulation

In the simulation experiment, a spotlight mode SAR echo data is simulated with a 3×3 point targets array being arranged in the simulation scene. The geometry of the scene is presented in Fig. 5. The satellite orbit is generated based on the two-body model. The motion of the satellite is simulated between and during transmission and reception. The simulation parameters are listed in Table II. The synthetic aperture time is 10 s, resulting in intolerable error introduced by third-order and higher-order terms of range history. The pulse duration is 35 us, which will illustrate the influence of fast-time effect clearly. The full-aperture algorithm TSPA and the proposed algorithm are used to process the raw data, respectively. In order to compare the focusing performance between the two algorithms, the quantitative results of all targets are evaluated. The target P5 is in the center of the whole scene and is affected by the minimum distortion. The corner targets (P1, P3, P7, and P9) are affected by the maximum
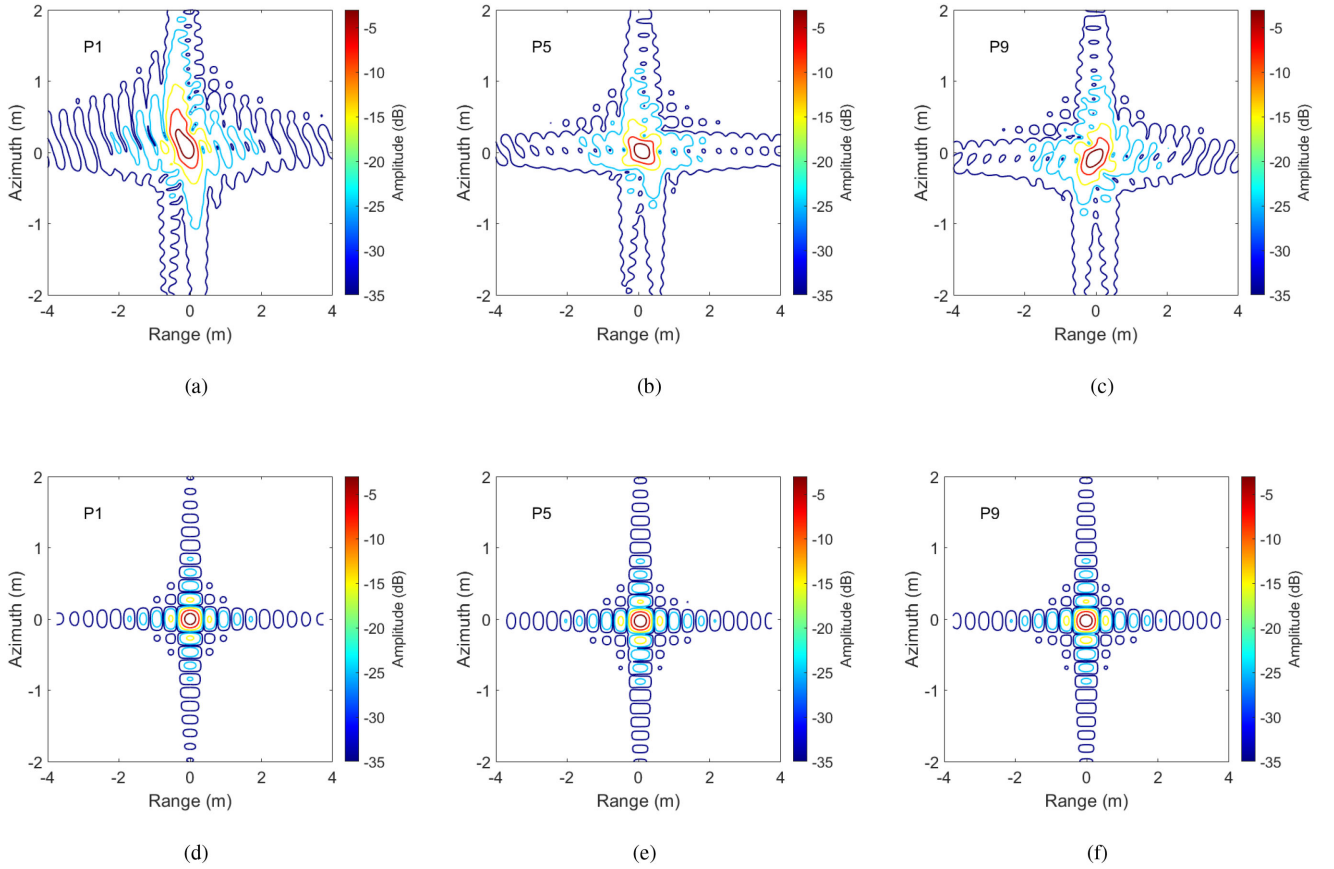
Fig. 6. Comparative results of targets P1, P5, and P9. Imaging results of (a) target P1, (b) target P5, and (c) target P9 by using TSPA, without start–stop correction and curved orbit correction. Imaging results of (d) target P1, (e) target P5, and (f) target P9 by using the proposed algorithm.

TABLE II
SPOTLIGHT SAR SIMULATION PARAMETERS

Parameter	Value
Carrier frequency	9.6 GHz
Incidence angle	30°
Range bandwidth	700 MHz
Range sampling frequency	840 MHz
Pulse duration	35 μs
PRF	6000 Hz
Synthetic aperture time	10 s

distortion. Once P1 and P9 are investigated, an analysis of P3 and P7 is unnecessary. For simplicity, only P1, P5, and P9 are investigated in the article. The interpolated contours of P1, P5, and P9 focused with the traditional and the proposed algorithm are shown in Fig. 6. Moreover, quantitative results of the imaging quality are listed in Table III, including the impulse response width (IRW), the peak sidelobe ratio (PSLR), and the integration sidelobe ratio (ISLR) in range and azimuth directions.

The theoretical azimuth resolution is about 0.166 m. The theoretical range resolution is about 0.3795 m. As shown in the processing results, due the curved orbit and the start–stop approximation, the targets P1, P5, and P9 suffer from resolution reduction and impulse response function (IRF) profile distortion by using the TSPA. However, by implementing the proposed

algorithm, the targets P1, P5, and P9 have a good focusing performance, which verifies the feasibility of the proposed algorithm.

In order to show how the curved-orbit and the start–stop assumption affect the image quality respectively, some intermedia results are shown in Fig. 7. Fig. 7(a) shows the imaging result of P5 without correction of error introduced by start–stop approximation (the error introduced by the curved orbit is corrected). Fig. 7(b) and (c) are the range profile and azimuth profile of the imaging result in Fig. 7(a), respectively. The IRF profile distortion of target is mainly caused by "fast-time" effect. As stated in [38], the shift property of the Fourier transform can be used to analyze "fast-time" effect

$$\mathcal{F}^{-1}\left[S_a\left(f_\tau, f_\eta\right) \exp\left(j2\pi \frac{f_\eta}{K_r} f_\tau\right)\right] = S_a\left(\frac{f_\eta}{K_r} + \tau, f_\eta\right) \tag{17}$$

where $\mathcal{F}^{-1}$ denotes the inverse Fourier transform in range, $S_a(f_\tau, f_\eta)$ is the Fourier transform of $S_a(\tau, f_\eta)$ in range. Equation (17) indicates that there exists an azimuth-frequency-dependent residual range migration correction term f_η/K_r in range Doppler domain. The IRF bifurcates in range and azimuth directions due to "fast-time" effect. Although the PSLR and the ISLR of the target in Fig. 7(a) in range direction are better than the target in Fig. 6(e), they are at the expense of range

TABLE III
EVALUATION OF IMAGING QUALITY IN SIMULATION EXPERIMENT

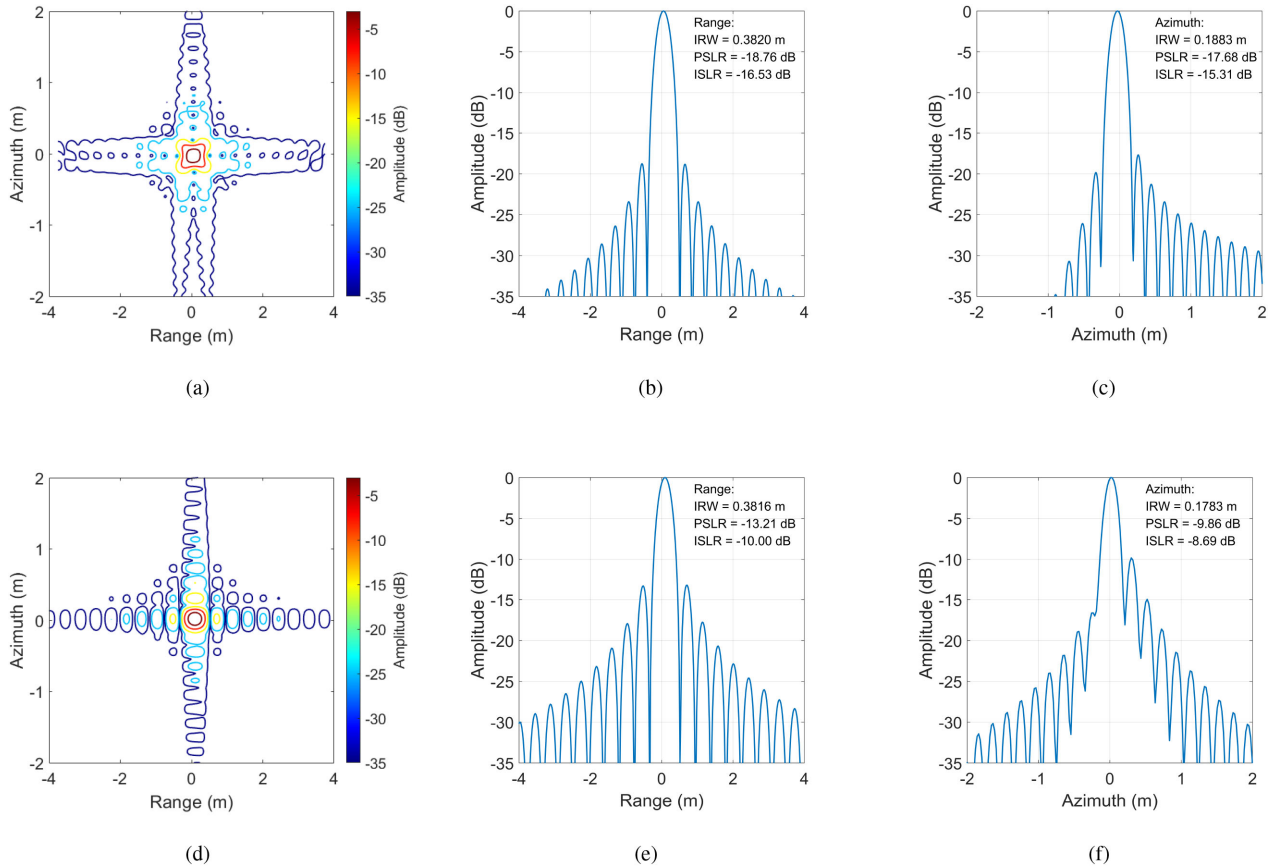| Methods	Targets	Azimuth			Range		
		IRW(m)	PSLR(dB)	ISLR(dB)	IRW(m)	PSLR(dB)	ISLR(dB)
Two-step Processing Approach	P1	0.2897	-7.28	-8.53	0.3900	-12.93	-10.52
	P5	0.2033	-12.60	-12.25	0.4179	-17.49	-14.88
	P9	0.2117	-9.47	-10.23	0.4151	-16.78	-14.09
Proposed Algorithm	P1	0.1672	-12.93	-9.86	0.3784	-13.24	-10.18
	P5	0.1672	-13.32	-10.17	0.3793	-13.26	-10.19
	P9	0.1664	-13.26	-10.22	0.3810	-13.27	-10.19

Fig. 7. (a) Imaging result of target P5 without start-stop correction. (b) Range profile. (c) Azimuth profile.(d) Imaging result of target P5 without the correction of curved orbit. (e) Range profile. (f) Azimuth profile.

resolution reduction. The IRW of target in Fig. 7(a) in range direction is 0.3820 m while it is 0.3793 m in Fig. 6(e) in the range direction. Fig. 7 (d) shows the imaging result of P5 without correction of error introduced by the curved orbit (the error introduced by start-stop approximation is corrected). The IRF profile distortion of target is caused by the error introduced by third- and higher-order terms of range history. As Fig. 7(f) shows, the error degrades the azimuth resolution and introduces asymmetric sidelobes.

B. Spaceborne SAR Data Experiment

In this experiment, the spaceborne SAR data required by GF-3 satellite is used to verify the feasibility of the proposed algorithm.

A high-resolution SAR focusing experiment based on GF-3 spotlight data is addressed. Some parameters of the data are listed in Table IV. The steering angle range is $[-1.78°, 1.78°]$ in this spotlight data. The synthetic aperture time is 8.58 s. And the theoretical azimuth resolution is about 0.396 m. The theoretical range resolution is about 0.889 m. After processing of the data using the proposed algorithm, the result is shown in Fig. 8.

Since, the spotlight experiment mentioned above is not a regular mode of GF-3 satellite, there are no calibration experiment in the calibration field at the commissioning phase. The scene is very complicated, and it is difficult to find an ideal corner reflector. In order to analyze the quality of the focused image produced by our approach, three point targets T1 and T2 which are distributed in the scene are treated as approximate ideal
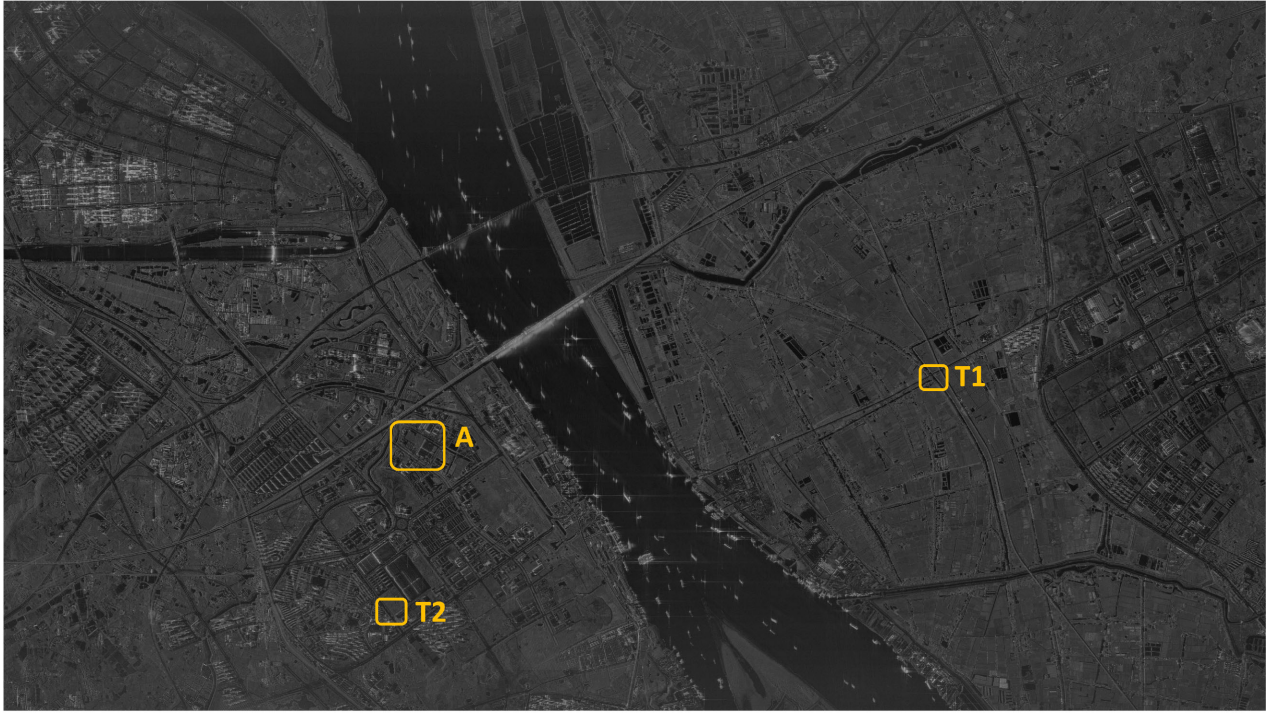
Fig. 8. Reflectivity image of the GF-3 spotlight acquisition acquired over Nanjing, China (vertical azimuth, horizontal range).

TABLE IV
SOME PARAMETERS OF GF-3 SPOTLIGHT MODE

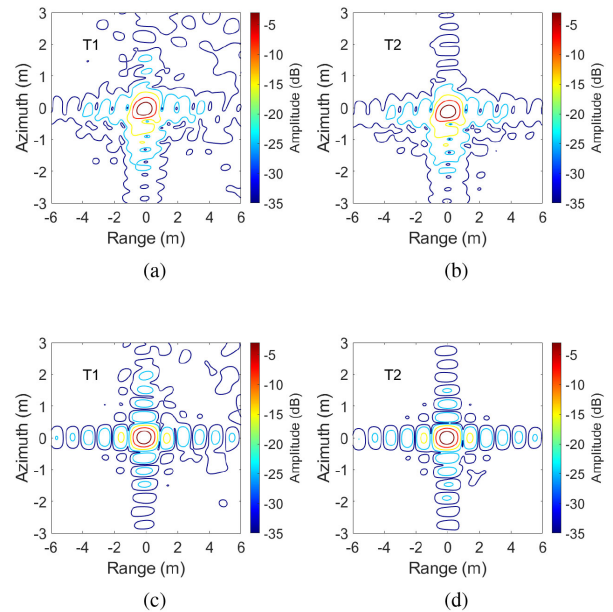| Parameter	Value
Carrier frequency	5.4 GHz
Look angle	33.75°
Incidence angle	38.51°
Range bandwidth	240 MHz
Range sampling frequency	266.67 MHz
Pulse duration	45 μs
Azimuth bandwidth	19380 Hz
PRF	3742.80 Hz
Azimuth steering range	±1.78°
Synthetic aperture time	8.58 s

Fig. 9. Comparative results of targets T1 and T2 in the real scene. No sidelobe suppression was performed. Imaging results of (a) target T1 and (b) target T2 by using TSPA, without start–stop correction and curved orbit correction. Imaging results of (c) target T1 and (d) target T2 by using the proposed algorithm.

corner reflectors. The interpolated contours of T1 and T2 focused with the traditional and the proposed algorithm are shown in Fig. 9. Moreover, quantitative results of the imaging quality are listed in Table V, including IRW, PSLR, and ISLR in range and azimuth directions.

As shown in the processing results, due to the curved orbit and the start-stop approximation, the targets T1 and T2 suffer from resolution reduction and IRF profile distortion by using the TSPA. The IRW of T1 in Fig. 9(a) in range direction is 0.9477 m, which is more than 6.6% compared with the theoretical IRW. The error introduced by "fat-time" effect in 2-D frequency is shown in Fig. 10(a). The error reaches ±33 degrees at the edges of the spectrum. If not corrected, the imaging result of T1 can be seen in Fig. 10(b). The IRF bifurcates in range and azimuth directions due to "fast-time" effect, which is similar to simulation experiment. The IRW of the target T1 in Fig. 10(b) in range direction is 0.9203 m while it is 0.892 m in Fig. 9(c).

As shown in Fig. 9(c) and (d), by implementing the proposed algorithm, the interpolated contours of T1 and T2 have good focusing performance. The IRWs of T1 and T2 in range direction are 0.892 and 0.898 m, respectively, which are broadly consistent with theoretical IRW (0.889 m). The theoretical IRW in azimuth direction is 0.396 m. As shown in Table V, the IRWs of T1 and

TABLE V
EVALUATION OF IMAGING QUALITY IN GF-3 DATA EXPERIMENT

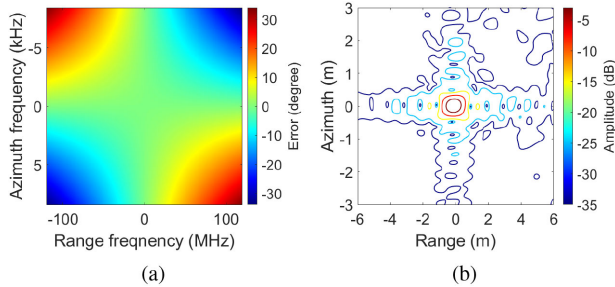| Methods	Targets	Azimuth			Range		
		IRW(m)	PSLR(dB)	ISLR(dB)	IRW(m)	PSLR(dB)	ISLR(dB)
Two-step Processing Approach	T1	0.450	-8.65	-9.30	0.948	-16.06	-13.34
	T2	0.447	-8.75	-9.73	0.959	-16.10	-13.41
Proposed Algorithm	T1	0.399	-15.18	-12.26	0.892	-13.17	-10.28
	T2	0.396	-15.77	-12.77	0.898	-13.26	-10.34

Fig. 10. (a) Error introduced by "fast-time" effect in 2-D-frequency domain. (b) Imaging result of target T1 without correction of the error introduced by "fast-time" effect.
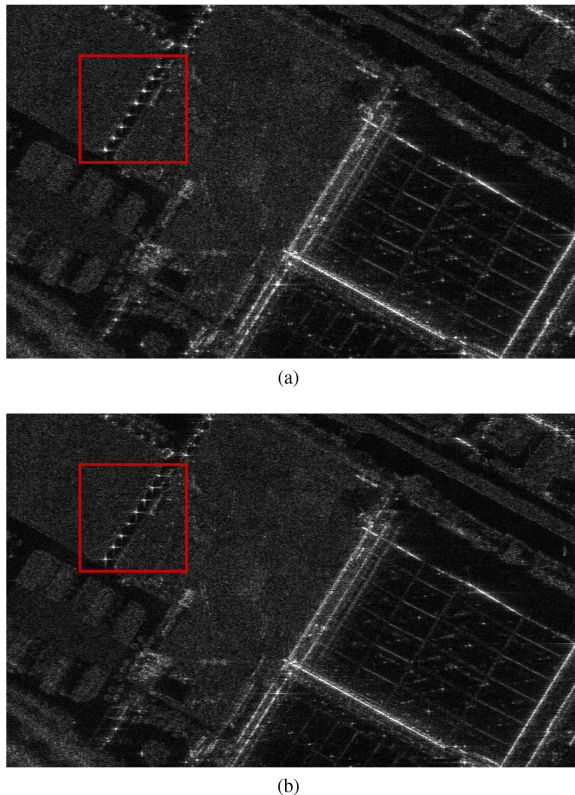

(a)

(b)

Fig. 11. Imaging results of local area A in Fig. 8 by using (a) TSPA and (b) proposed algorithm.

T2 in azimuth direction are 0.399 and 0.396 m, respectively, which are also broadly consistent with the theoretical analysis. In the experiment, the atmospheric effect is not corrected. The accuracy of the orbit parameters will also influence the orbit error correction. The IRFs of three targets can also be influenced by the topography variations. Furthermore, surroundings of three targets will also influence their IRFs. As a result, the IRFs of three targets are not the same as IRF of the ideal corner reflector. However, compared with the results of TSPA and the proposed algorithm, the proposed algorithm has a better focusing performance. The local area A in Fig. 9 is also shown in Fig. 11 for comparison. Compared with Fig. 11(a), Fig. 11(b) is more clear and has better focusing quality, which verifies the feasibility of the proposed algorithm.

V. CONCLUSION

Modern SAR systems are characterized by high resolution and wide swath coverage. Spaceborne SAR systems are unique in providing high resolution weather-independent images of the earth surface. The capabilities of high azimuth resolution in the spotlight are accompanied by new challenges, such as Doppler spectrum aliasing, curved orbit, and significant error in start-stop approximation. For high-resolution spaceborne SAR system, all the challenges mentioned above should be considered.

In this article, an imaging algorithm is proposed for very high resolution spaceborne spotlight mode. First, the initial step of TSPA is used to get a high azimuth sampling rate which is higher than PRF to avoid the Doppler spectrum aliasing. Then, the "fast-time" effect of start-stop approximation is corrected in 2-D frequency domain. Finally, the BPA is used to correct the error introduced by the curved orbit and the "slow-time" effect of start–stop approximation. The simulation results confirm that the proposed algorithm has good performance. The experimental results of spaceborne SAR data acquired by GF-3 SAR system demonstrate the feasibility of the proposed algorithm. The proposed algorithm can be applied to spotlight modes of other high resolution spaceborne SAR systems. The drawback of the proposed method is its huge computation. One of the solutions may be to combine the proposed method with fast factorized BPA [32]. The proposed algorithm can also be applied to sliding spotlight modes with a minor revision. The GF-3 experiment lays a good foundation for the development of new higher-resolution SAR. Based on the algorithm proposed in this article, many works can be continually done. We fill focus on the correction of atmospheric effect, topography variations, and accelerating algorithms in the future.

reviewers for their constructive comments and suggestions which helped in improving the readability of this article.

REFERENCES

[1] A. Moreira, P. Prats-Iraola, M. Younis, G. Krieger, I. Hajnsek, and K. P. Papathanassiou, "A tutorial on synthetic aperture radar," *IEEE Geosci. Remote Sens. Mag.*, vol. 1, no. 1, pp. 6–43, Mar. 2013.

[2] J. Mittermayer, A. Moreira, and O. Lofeld, "Spotlight SAR data processing using the frequency scaling algorithm," *IEEE Trans. Geosci. Remote Sens.*, vol. 37, no. 5, pp. 2198–2214, Sep. 1999.

[3] S. Tang, L. Zhang, and H. So, "Focusing high-resolution highly-squinted airborne SAR data with maneuvers," *Remote Sens.*, vol. 10, no. 6, Jun. 2018, Art. no. 862.

[4] D. An, X. Huang, J. Tian, and Z. Zhou, "Extended two-step focusing approach for squinted spotlight SAR imaging," *IEEE Trans. Geosci. Remote Sens.*, vol. 50, no. 7, pp. 2889–2900, Jul. 2012.

[5] W. Yuan, G. C. Sun, C. Yang, J. Yang, M. Xing, and B. Zheng, "Processing of very high resolution spaceborne sliding spotlight SAR data using velocity scaling," *IEEE Trans. Geosci. Remote Sens.*, vol. 54, no. 3, pp. 1505–1518, Mar. 2016.

[6] J. Mittermayer, S. Wollstadt, P. Prats-Iraola, and R. Scheiber, "The TerraSAR-X staring spotlight mode concept," *IEEE Trans. Geosci. Remote Sens.*, vol. 52, no. 6, pp. 3695–3706, Jun. 2014.

[7] B. Han *et al.*, "The GF-3 SAR data processor," *Sensors*, vol. 18, no. 3, Mar. 2018, Art. no. 835.

[8] M. Deng, G. Zhang, R. Zhao, S. Li, and J. Li, "Improvement of Gaofen-3 absolute positioning accuracy based on cross-calibration," *Sensors*, vol. 17, no. 12, 2017, Art. no. 2903.

[9] M. Zheng, H. Yan, L. Zhang, W. Yu, Y. Deng, and R. Wang, "Research on strong clutter suppression for Gaofen-3 dual-channel SAR/GMTI," *Sensors*, vol. 18, no. 4, 2018, Art. no. 978.

[10] Q. Zhang, "System design and key technologies of the GF-3 satellite," *Acta Geodaetica Et Cartographica Sinica*, vol. 46, no. 3, pp. 269–277, Mar. 2017.

[11] J. Sun, W. Yu, and Y. Deng, "The SAR payload design and performance for the GF-3 mission," *Sensors*, vol. 17, no. 10, Oct. 2017, Art. no. 2419.

[12] Z. Fan, X. Yao, H. Tang, Y. Qiang, Y. Hu, and B. Lei, "Multiple mode SAR raw data simulation and parallel acceleration for Gaofen-3 mission," *IEEE J. Sel. Topics Appl. Earth Observ. Remote Sens.*, vol. 11, no. 6, pp. 2115–2126, Jun. 2018.

[13] T. Wang, G. Zhang, L. Yu, R. Zhao, M. Deng, and K. Xu, "Multi-mode GF-3 satellite image geometric accuracy verification using the RPC model," *Sensors*, vol. 17, no. 9, 2017, Art. no. 2005.

[14] M. Shang *et al.*, "A high-resolution SAR focusing experiment based on GF-3 staring data," *Sensors*, vol. 18, no. 4, 2018, Art. no. 943.

[15] P. Prats-Iraola *et al.*, "On the processing of very high resolution spaceborne SAR data," *IEEE Trans. Geosci. Remote Sens.*, vol. 52, no. 10, pp. 6003–6016, Oct. 2014.

[16] P. Prats, R. Scheiber, J. Mittermayer, A. Meta, and A. Moreira, "Processing of sliding spotlight and TOPS SAR data using baseband Azimuth scaling," *IEEE Trans. Geosci. Remote Sens.*, vol. 48, no. 2, pp. 770–780, Feb. 2010.

[17] F. He, Q. Chen, Z. Dong, and Z. Sun, "Processing of ultrahigh-resolution spaceborne sliding spotlight SAR data on curved orbit," *IEEE Trans. Aerosp. Electron. Syst.*, vol. 49, no. 2, pp. 819–839, Apr. 2013.

[18] J. Mittermayer, R. Lord, and E. Borner, "Sliding spotlight SAR processing for TerraSAR-X using a new formulation of the extended chirp scaling algorithm," in *IEEE Int. Geosci. Remote Sens. Symp.*, 2004.

[19] R. Lanari, S. Zoffoli, E. Sansosti, G. Fornaro, and F. Serafino, "New approach for hybrid strip-map/spotlight SAR data focusing," *IEEE Proc. - Radar, Sonar Navigation*, vol. 148, no. 6, pp. 363–372, Dec. 2001.

[20] R. Lanari, M. Tesauro, E. Sansosti, and G. Fornaro, "Spotlight SAR data focusing based on a two-step processing approach," *IEEE Trans. Geosci. Remote Sens.*, vol. 39, no. 9, pp. 1993–2004, Sep. 2001.

[21] G. Sun, M. Xing, W. Yong, Y. Wu, Y. Wu, and B. Zheng, "Sliding spotlight and TOPS SAR data processing without subaperture," *IEEE Geosci. Remote Sens. Lett.*, vol. 8, no. 6, pp. 1036–1040, Nov. 2011.

[22] X. Wei, Y. Deng, P. Huang, and R. Wang, "Full-aperture SAR data focusing in the spaceborne squinted sliding-spotlight mode," *IEEE Trans. Geosci. Remote Sens.*, vol. 52, no. 8, pp. 4596–4607, Aug. 2014.

[23] D. Meng, C. Ding, D. Hu, X. Qiu, and X. Ning, "On the processing of very high resolution spaceborne SAR data: A chirp-modulated back projection approach," *IEEE Trans. Geosci. Remote Sens.*, vol. 56, no. 1, pp. 191–201, Jan. 2018.

[24] R. Bamler, "A comparison of range-doppler and wavenumber domain SAR focusing algorithms," *IEEE Trans. Geosci. Remote Sens.*, vol. 30, no. 4, pp. 706–713, Jul. 1992.

[25] I. G. Cumming and F. H. Wong, *Digital Processing of Synthetic Aperture Radar Data: Algorithms and Implementation*. Norwood, MA, USA: Artech House, 2005.

[26] Y. Luo, B. Zhao, X. Han, R. Wang, H. Song, and Y. Deng, "A novel high-order range model and imaging approach for high-resolution LEO SAR," *IEEE Trans. Geosci. Remote Sens.*, vol. 52, no. 6, pp. 3473–3485, Jun. 2014.

[27] K. Eldhuset, "A new fourth-order processing algorithm for spaceborne SAR," *IEEE Trans. Aerosp. Electron. Syst.*, vol. 34, no. 3, pp. 824–835, Sep. 1998.

[28] Z. Yu, S. Wang, and Z. Li, "An imaging compensation algorithm for spaceborne high-resolution SAR based on a continuous tangent motion model," *Remote Sens.*, vol. 8, no. 3, 2016, Art. no. 223.

[29] A. Ribalta, "Time-domain reconstruction algorithms for FMCW-SAR," *IEEE Geosci. Remote Sens. Lett.*, vol. 8, no. 3, pp. 396–400, May 2011.

[30] M. Soumekh, *Synthetic Aperture Radar Signal Processing With MATLAB Algorithms*. New York, NY, USA: Wiley, 1999.

[31] M. D. Desai and W. K. Jenkins, "Convolution backprojection image reconstruction for spotlight mode synthetic aperture radar," *IEEE Trans. Geosci. Remote Sens.*, vol. 1, no. 4, pp. 505–517, Oct. 1992.

[32] L. M. H. Ulander, H. Hellsten, and G. Stenstrom, "Synthetic aperture radar processing using fast factorized back-projection," *IEEE Trans. Aerosp. Electron. Syst.*, vol. 39, no. 3, pp. 760–776, Jul. 2003.

[33] J. Shi, L. Ma, and X. Zhang, "Streaming BP for non-linear motion compensation SAR imaging based on GPU," *IEEE J. Sel. Topics Appl. Earth Observ. Remote Sens.*, vol. 6, no. 4, pp. 2035–2050, Aug. 2013.

[34] F. Zhang, G. Li, W. Li, W. Hu, and Y. Hu, "Accelerating spaceborne SAR imaging using multiple CPU/GPU deep collaborative computing," *Sensors*, vol. 16, no. 4, 2016, Art. no. 494.

[35] H. Zhang, J. Tang, R. Wang, Y. Deng, W. Wang, and N. Li, "An accelerated backprojection algorithm for monostatic and bistatic SAR processing," *Remote Sens.*, vol. 10, no. 1, 2018, Art. no. 140.

[36] Y. Can Evren, Y. Birsen, and C. Margaret, "Bistatic synthetic aperture radar imaging for arbitrary flight trajectories," *IEEE Trans. Image Process.*, vol. 17, no. 1, pp. 84–93, Jan. 2008.

[37] S. Duque, H. Breit, U. Balss, and A. Parizzi, "Absolute height estimation using a single TerraSAR-X staring spotlight acquisition," *IEEE Geosci. Remote Sens. Lett.*, vol. 12, no. 8, pp. 1735–1739, Aug. 2015.

[38] L. Yan *et al.*, "Echo model analyses and imaging algorithm for high-resolution SAR on high-speed platform," *IEEE Trans. Geosci. Remote Sens.*, vol. 50, no. 3, pp. 933–950, Mar. 2012.

[39] M. D. Bisceglie, M. D. Santo, C. Galdi, R. Lanari, and N. Ranaldo, "Synthetic aperture radar processing with GPGPU," *IEEE Signal Process. Mag.*, vol. 27, no. 2, pp. 69–78, Mar. 2010.

Da Liang (Student Member, IEEE) received the B.S. degree from Nankai University, Tianjin, China, in 2016. He is currently working toward the Ph.D. degree with the Space Microwave Remote Sensing System Department, Aerospace Information Research Institute, Chinese Academy of Sciences, Beijing, China.

He is currently with the University of Chinese Academy of Sciences, Beijing, China. His research interests include synthetic aperture radar (SAR) imaging, SAR internal calibration, synchronization of bistatic SAR system, and signal processing.
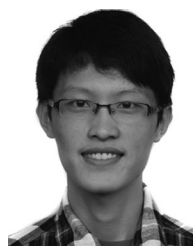
Heng Zhang (Member, IEEE) received the B.S. degree from Nanjing University, Nanjing, China, in 2013, and the Ph.D. degree in communication and information systems from the University of Chinese Academy of Sciences, Beijing, China, in 2018.

In 2018, he joined the Aerospace Information Research Institute, Chinese Academy of Sciences, Beijing, China. His research interests include bistatic synthetic aperture radar imaging and interferometry.

Tingzhu Fang was born in Anhui, China, in 1996. He received the B.S. degree from Central South University, Changsha, China, in 2017. He is currently working toward the Ph.D. degree with the Space Microwave Remote Sensing System Department, Aerospace Information Research Institute, Chinese Academy of Sciences, Beijing, China.

He is currently with the University of Chinese Academy of Sciences, Beijing, China. His research interests include synthetic aperture radar imaging and signal processing.

Yunkai Deng (Member, IEEE) received the M.S. degree in electrical engineering from the Beijing Institute of Technology, Beijing, China, in 1993.

In 1993, he joined the Institute of Electronics, Chinese Academy of Sciences (IECAS), Beijing, China, where he was involved in antenna design, microwave circuit design, and spaceborne/airborne synthetic-aperture radar (SAR) technology. Since 1993, he has been a Research Fellow with the Department of Space Microwave Remote Sensing System, IECAS. He has been the Leader of several spaceborne/airborne SAR programs and developed some key technologies of spaceborne/airborne SAR. Since 2012, he has been a Principal Investigator with the Helmholtz-Chinese Academy of Sciences (CAS) Joint Research Group, Beijing, China, concerning spaceborne microwave remote sensing for prevention and forensic analysis of natural hazards and extreme events. He is currently a Research Scientist with the University of Chinese Academy of Sciences. He has authored or co-authored more than 100 articles since 2002, of which more than 100 are peer-reviewed and well-known journal articles. His research interests include spaceborne/airborne SAR technology for advanced modes, multifunctional radar imaging, and microwave circuit design.

Mr. Deng is a member of the Scientific Board. He was the recipient of several prizes, including the First and Second Class Rewards of National Defense Science and Technology Progress, in 2007, the First Class Reward of the National Scientific and Technological Progress, in 2008, the achievements of the Outstanding Award of the CAS, in 2009, and the First Class Reward of Army Science and Technology Innovation, in 2016, for his outstanding contribution in the SAR field.

Weidong Yu (Member, IEEE) was born in Henan, China, in 1969. He received the M.Sc. and the Ph.D. degrees in electrical engineering from the Nanjing University of Aeronautics and Astronautics, Nanjing, China, in 1994 and 1997, respectively.

Since 1997, he has been with the Institute of Electronics, Chinese Academy of Sciences (IECAS), Beijing, China, where he became a Professor of Communication and Information Systems, in 2000. He has been the Chief Designer for several synthetic aperture radar (SAR) systems. He is currently the Director of Space Microwave Remote Sensing System Department, Aerospace Information Research Institute, Chinese Academy of Sciences. His research interests include spaceborne and airborne SAR system design and their signal processing.
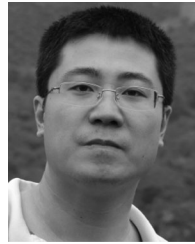
Lei Zhang was born in Jilin, China, in 1985. He received the Ph.D. degree from the Institute of Electronics, Chinese Academy of Sciences, Beijing, China, in 2014.

He is currently an Associate Research Fellow with the Aerospace Information Research Institute, Chinese Academy of Sciences. His research interests include high resolution synthetic aperture radar imaging and signal processing.

Huaitao Fan (Member, IEEE) received the B.S. degree in electronic information science and technology from the Ocean University of China, Qingdao, China, in 2012 and the Ph.D. degree from the University of Chinese Academy of Sciences, Beijing, China, in 2017.

In 2017, he joined the Aerospace Information Research Institute, Chinese Academy of Sciences, Beijing, China. His research interests include multi-channel in azimuth synthetic aperture radar imaging.